Simultaneous dual-wavelength imaging of nonfluorescent tissues with 3D subdiffraction photothermal microscopy

Jun Miyazaki,[1,2] **Hiromichi Tsurui,**[3] **Koshi Kawasumi,**[1] **and Takayoshi Kobayashi**[1,2,4,5,*]

[1] *Advanced Ultrafast Laser Research Center, The University of Electro-Communications, 1-5-1 Chofugaoka, Chofu, Tokyo, 182-8585, Japan*
[2] *JST, CREST, K' Gobancho, 7, Gobancho, Chiyoda-ku, Tokyo 102-0076, Japan*
[3] *Department of Pathology, Juntendo University School of Medicine, 2-1-1, Hongo, Bunkyo-ku, Tokyo 113-8421, Japan*
[4] *Department of Electrophysics, National Chiao-Tung University, Hsinchu 300, Taiwan*
[5] *Institute of Laser Engineering, Osaka University, 2-6 Yamada-oka, Suita, Osaka 565-0971, Japan*
[*] *kobayashi@ils.uec.ac.jp*

Abstract: Multi-wavelength microscopic imaging is essential to visualize a variety of nanoscale cellular components with high specificity and high spatial resolution. However, previous techniques are based on fluorescence, and thus cannot visualize nonfluorescent species, which are much less suffered from photodamage or photobleaching and hence are intrinsically useful in wider range of optical microscopy. Here, we show that simultaneous multi-wavelength imaging of nonfluorescent species can be achieved with the use of a photothermal microscope. Dual-wavelength subdiffraction imaging of biological tissues stained with hematoxylin and eosin is demonstrated. Three-dimensional label-free imaging of mouse melanoma tissue section is also presented to demonstrate the effectiveness of the enhanced spatial resolution. Our technique can be implemented using cost-effective and compact laser diodes and is applicable for various types of both fluorescent and nonfluorescent tissues.

OCIS codes: (180.0180) Microscopy; (140.2020) Diode lasers; (100.6640) Superresolution.

References and links

1. L. Cognet, C. Tardin, D. Boyer, D. Choquet, P. Tamarat, and B. Lounis, "Single metallic nanoparticle imaging for protein detection in cells," Proc. Natl. Acad. Sci. U.S.A. **100**(20), 11350–11355 (2003).
2. S. Berciaud, D. Lasne, G. A. Blab, L. Cognet, and B. Lounis, "Photothermal heterodyne imaging of individual metallic nanoparticles: Theory versus experiment," Phys. Rev. B **73**(4), 045424 (2006).
3. V. Octeau, L. Cognet, L. Duchesne, D. Lasne, N. Schaeffer, D. G. Fernig, and B. Lounis, "Photothermal absorption correlation spectroscopy," ACS Nano **3**(2), 345–350 (2009).
4. R. Radünz, D. Rings, K. Kroy, and F. Cichos, "Hot Brownian particles and photothermal correlation spectroscopy," J. Phys. Chem. A **113**(9), 1674–1677 (2009).
5. P. M. R. Paulo, A. Gaiduk, F. Kulzer, S. F. G. Krens, H. P. Spaink, T. Schmidt, and M. Orrit, "Photothermal Correlation Spectroscopy of Gold Nanoparticles in Solution," J. Phys. Chem. C **113**(27), 11451–11457 (2009).
6. A. Gaiduk, P. V. Ruijgrok, M. Yorulmaz, and M. Orrit, "Detection limits in photothermal microscopy," Chem. Sci. **1**(3), 343–350 (2010).
7. A. Gaiduk, M. Yorulmaz, P. V. Ruijgrok, and M. Orrit, "Room-temperature detection of a single molecule's absorption by photothermal contrast," Science **330**(6002), 353–356 (2010).
8. D. A. Nedosekin, E. V. Shashkov, E. I. Galanzha, L. Hennings, and V. P. Zharov, "Photothermal multispectral image cytometry for quantitative histology of nanoparticles and micrometastasis in intact, stained and selectively burned tissues," Cytometry A **77A**(11), 1049–1058 (2010).
9. S. Lu, W. Min, S. Chong, G. R. Holtom, and X. S. Xie, "Label-free imaging of heme proteins with two-photon excited photothermal lens microscopy," Appl. Phys. Lett. **96**(11), 113701 (2010).
10. C. Leduc, J. M. Jung, R. P. Carney, F. Stellacci, and B. Lounis, "Direct investigation of intracellular presence of gold nanoparticles via photothermal heterodyne imaging," ACS Nano **5**(4), 2587–2592 (2011).
11. W.-S. Chang and S. Link, "Enhancing the sensitivity of single-particle photothermal imaging with thermotropic liquid crystals," J. Phys. Chem. Lett. **3**(10), 1393–1399 (2012).

#228731 - $15.00 USD Received 28 Nov 2014; revised 19 Jan 2015; accepted 26 Jan 2015; published 5 Feb 2015
(C) 2015 OSA 9 Feb 2015 | Vol. 23, No. 3 | DOI:10.1364/OE.23.003647 | OPTICS EXPRESS 3647

12. C. Leduc, S. Si, J. Gautier, M. Soto-Ribeiro, B. Wehrle-Haller, A. Gautreau, G. Giannone, L. Cognet, and B. Lounis, “A highly specific gold nanoprobe for live-cell single-molecule imaging,” Nano Lett. **13**(4), 1489–1494 (2013).
13. M. Selmke and F. Cichos, “Photothermal single particle Rutherford scattering microscopy,” Phys. Rev. Lett. **110**(10), 103901 (2013).
14. J. Miyazaki, H. Tsurui, K. Kawasumi, and T. Kobayashi, “Optimal detection angle in sub-diffraction resolution photothermal microscopy: application for high sensitivity imaging of biological tissues,” Opt. Express **22**(16), 18833–18842 (2014).
15. M. Selmke, A. Heber, M. Braun, and F. Cichos, “Photothermal single particle microscopy using a single laser beam,” Appl. Phys. Lett. **105**(1), 013511 (2014).
16. P. Vermeulen, L. Cognet, and B. Lounis, “Photothermal microscopy: optical detection of small absorbers in scattering environments,” J. Microsc. **254**(3), 115–121 (2014).
17. Y. Ozeki, W. Umemura, Y. Otsuka, S. Satoh, H. Hashimoto, K. Sumimura, N. Nishizawa, K. Fukui, and K. Itoh, “High-speed molecular spectral imaging of tissue with stimulated Raman scattering,” Nat. Photonics **6**(12), 845–850 (2012).
18. J. Miyazaki, H. Tsurui, A. Hayashi-Takagi, H. Kasai, and T. Kobayashi, “Sub-diffraction resolution pump-probe microscopy with shot-noise limited sensitivity using laser diodes,” Opt. Express **22**(8), 9024–9032 (2014).
19. J. Miyazaki, K. Kawasumi, and T. Kobayashi, “Frequency domain approach for time-resolved pump-probe microscopy using intensity modulated laser diodes,” Rev. Sci. Instrum. **85**(9), 093703 (2014).
20. J. Miyazaki, K. Kawasumi, and T. Kobayashi, “Resolution improvement in laser diode-based pump-probe microscopy with an annular pupil filter,” Opt. Lett. **39**(14), 4219–4222 (2014).
21. W. Denk, J. H. Strickler, and W. W. Webb, “Two-photon laser scanning fluorescence microscopy,” Science **248**(4951), 73–76 (1990).
22. A. Penzkofer, A. Beidoun, and M. Daiber, “Intersystem-crossing and excited-state absorption in eosin-Y solutions determined by picosecond double pulse transient absorption-measurements,” J. Lumin. **51**(6), 297–314 (1992).
23. A. Gaiduk, P. V. Ruijgrok, M. Yorulmaz, and M. Orrit, “Making gold nanoparticles fluorescent for simultaneous absorption and fluorescence detection on the single particle level,” Phys. Chem. Chem. Phys. **13**(1), 149–153 (2010).

---

1. Introduction

Photothermal microscopy is an efficient method for observing molecules or nanomaterials using only their optical absorption [1–16]. Typically, two laser beams (pump and probe beams) are incident on the sample through a focusing lens. The pump beam increases the temperature around the optical absorbing sample in the focal spot range. This results in local refractive index variations (typically ~10^{-5} - 10^{-3} with ΔT = 0.1-10 K) [6, 7] and induces deflection of the probe beam. Variation in refractive index is detected as a change in probe beam transmissivity by a lock-in detection scheme with a modulated pump beam. This technique has been applied for biological imaging, such as in imaging biological tissues using gold nanoparticles [1, 10, 12], evaluating the hydrodynamic properties of cytosol with photothermal absorption correlation spectroscopy [3–5] and label-free and three-dimensional imaging of haeme proteins with two-photon excitation [9]. However, previous photothermal imaging has been single color only, and multi-wavelength imaging with multiplex biomolecule labelling is needed to visualize a variety of cellular components in high specificity.

The photothermal signal is proportional to the absorption cross-section of the sample material [6, 7]. Thus, when the sample contains different species, the measured signal is given by the linear sum of the signals from the different species. If we know the number of species in the sample and their absorption spectra, the abundance of species may be determined from spectral images (images measured with different pump wavelengths) through the spectral unmixing procedure. For unknown spectra or materials, spectral images can be processed by blind unmixing based on principle or independent component analysis as with stimulated Raman scattering microscopy [17].

In the previous report, photothermal spectral images were acquired by using a wavelength-tunable optical parametric oscillator (OPO) as a pump beam with switching the laser wavelength and repeating scan [8]. However, this scheme would cause an error in performing spectral unmixing because of mechanical drift and photobleaching of the tissue. On the other hand, it is too costly to implement simultaneous multi-wavelength excitation using multiple OPOs. Thus, OPO-based schematic is not suited for multi-wavelength imaging. Recently, we implemented photothermal (pump-probe) microscopy using intensity-modulated laser diodes (LDs) in which shot-noise-limited sensitivity was achieved using a balanced detection with a dual modulation scheme [18,19]. As major advances have been made recently in high power blue to yellow emitting LDs make this scheme readily applicable to simultaneous multi-wavelength imaging by incorporating LDs with different wavelengths.

In this study, simultaneous dual-wavelength subdiffraction imaging of biological tissues stained with hematoxylin and eosin (H&E) is performed using two pump beams of LDs modulated at different frequencies. Highly reliable unmixed imagines reflecting the distribution of each species is obtained.

2. Experimental setup

2.1 Experimental system and principle of simultaneous dual-wavelength imaging

A 488-nm LD (Nichia NDS4216) and 532-nm diode pumped solid-state (DPSS) laser (Thorlabs, DJ525-40) were used for pumping, and a 660-nm LD (Mitsubishi ML101U29) was used for probing [Fig. 1(a)]. Each beam was collimated through a polarization maintaining single mode (SM) fiber for spatial mode filtering. Three beams were combined using dichroic mirrors. All beams were linearly polarized in the vertical plane. The combined beams were directed to the objective lens [40X, numerical aperture (NA) = 0.95]. The sample position was raster scanned using a three axis positioning stage driven by piezo actuators (Thorlabs, MAX311D). A condenser lens (Olympus, U-AAC) was used to collect the transmitted light. A narrowband filter matching the laser line was placed in front of the detector to filter out both the pump beam and fluorescence from the sample so that only the probe beam was detected. An iris diaphragm is used to adjust effective NA of the condenser lens for optimizing signal to noise ratio. An auto-balanced photodetector (Newfocus, Nirvana) was used to cancel the intensity fluctuation of the probe laser and achieve nearly shot noise limited sensitivity. A signal generator (Rigol DG4162) and an amplifier (Mini-circuit ZHL-6A +) were used to sinusoidally modulate the light intensity of the LD by controlling the injection current. The light intensity of the DPSS laser was externally modulated using an electro-optical modulator (LINOS LM020). To reduce the relative displacement between the images in the two channels, all beams were set to be collinear within the inter-beam angle of the order 10^{-5} rad. Furthermore, beam divergence angle was adjusted by changing the position of the doublet lens after the SM fiber so that the relative difference in divergence among the three beams was within the order of 10^{-5} rad. We also set up a confocal fluorescence detection scheme, wherein the fluorescence signal from the sample was detected by a photo-multiplier through a multimode fiber of 0.6 Airy units at a fluorescence wavelength of 600 nm.

Simultaneous dual-wavelength photothermal imaging is demonstrated using two pump beams modulated at different frequencies (ω_1 and ω_2) [Fig. 1(b)], with the probe beam modulated at ω_3. Photothermal signals are generated at beat frequencies of $|\omega_1 - \omega_3|$ and $|\omega_2 - \omega_3|$ by the bilinear interaction of the pump and probe fields at the sample. Each frequency component is demodulated using a lock-in amplifier referenced at the beat frequency. This dual-modulation scheme is capable of characterizing the microsecond to picosecond relaxation dynamics of sample species without using a high-frequency (wideband) detector and lock-in amplifier, whose principle and technique have been detailed in the previous paper [19]. This scheme also serves to eliminate the contribution of residual fluorescence that passes through the filter. To avoid channel interference, the beat frequency difference ($|\omega_1 - \omega_3| - |\omega_2 - \omega_3|$) is set (typically at 30 kHz) to be sufficiently larger than the inverse of the time constant of the lock-in amplifiers (1-2 kHz).

#228731 - $15.00 USD Received 28 Nov 2014; revised 19 Jan 2015; accepted 26 Jan 2015; published 5 Feb 2015

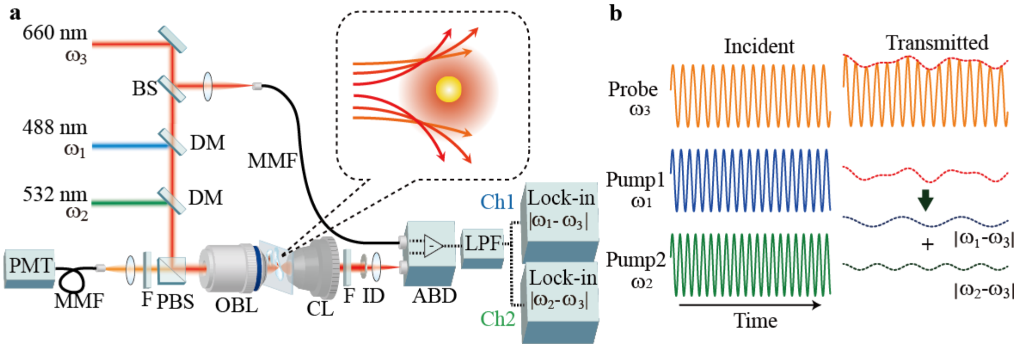

Fig. 1. Experimental setup and principle of dual-wavelength photothermal microscopy using intensity-modulated lasers. (a), Schematic of the experimental setup. DM: dichroic mirror, BS: beam splitter, PBS: polarization beam splitter, OBL: objective lens. CL: condenser lens, F: band-pass filter, ID: iris diaphragm, PMT: photomultiplier tube, MMF: multimode fiber, ABD: auto-balanced detector, LPF: low-pass filter. (b), Principle of dual-wavelength photothermal microscopy using intensity-modulated continuous-wave lasers. The pump-beam intensities are modulated at ω_1 and ω_2, and the probe beam intensity is modulated at ω_3. Beat signals are generated by the photothermal effect at the sample position, and they are detected using two lock-in amplifiers referenced at the beat frequencies.

2.2 Sample preparation

In skin melanoma imaging, B16 melanoma cells RCB-1283 (Riken Bio-Resource Centre) were cultured in RPMI-1640 supplemented with 10% FBS, 100 units/ml penicillin and 100 µg/ml streptomycin (Meiji Seika Kaisha Ltd.) at 37°C in a humidified atmosphere of 95% air and 5% CO2. A 50-µl suspension containing 0.5 million melanoma cells for each head was subcutaneously inoculated into female nude mice (6 weeks age) as five aliquots on the dorsal sides from the base of the tail to the neck. Tissues containing inoculated cells were fixed with 4% paraformaldehyde for 3 days, embedded in melted paraffin, sliced at 15-20 µm, extended on glass slides, and enclosed with a coverslip. H&E stained biological samples were purchased from Artec Co Ltd.

3. Results

3.1 Spatial resolution and optical sectioning capability

The spatial resolution of photothermal microscopy is considered to be dependent on the intensity profiles of the pump and probe beams and the refractive index profile at the focal point [2]. When the spatial extent of the modulating refractive index is much smaller than the spot size of the probe beam, the resolution (point spread function) is determined by the product of the intensity profiles of the pump and probe beams; thus, the spatial resolution is better than that of the diffraction-limited optical microscope [20]. Furthermore, this nonlinear signal provides optical sectioning capability as with confocal fluorescence and two-photon excitation microscopy [21].

The spatial resolution and displacement between the images in the two channels are examined by measuring single gold nanoparticles in the lateral and axial planes [Fig. 2(a)–2(e)]. The full width at half maximum value of the measured spot in the lateral plane is down to 234 nm, which is 34% smaller than the focal spot size of the probe beam ($0.51\lambda/NA = 354$ nm). Furthermore, the axial spot size is down to 510 nm, which is 35% smaller than the diffraction-limited axial size of the probe beam (689 nm). The displacements between the two channels are 29 nm in the lateral plane and 48 nm in the axial plane, which are within ~10% of the focal spot size. Use of an annular pupil filter further improves the lateral-plane spatial resolution, reaching nearly half of the diffraction-limited spot size; however, it reduces spatial resolution in the axial direction [20].

To demonstrate the effectiveness of the spatial resolution enhancement in photothermal microscopy, we performed label-free three-dimensional imaging of mouse melanoma [Figs. 2(f) and 2(g), Media 1]. 488-nm and 660-nm LDs are used for pump and probe beams, respectively. It can be clearly seen that the spatial resolution of photothermal image is better than that of bright-field image [Fig. 2(h)], which is measured by transmission-mode nearly confocal microscopy (Airy units 1.8) with the same probe beam. The distribution of melanin granules is clearly visualized in both planes in photothermal microscopy. Such three-dimensional structural information would be useful to differentiate melanoma from melanocytic nevi for diagnostic purposes. There was minimal damage to the sample after measurements.

Since the absorption spectrum of melanin is nearly flat in visible range, identical photothermal images are acquired in the simultaneous dual-wavelength measurement of mouse melanoma tissue section [Figs. 2(i) and 2(j)]. Furthermore, by measuring images with blocking either pump beam, we confirm that interference between the two channels is negligibly small (less than 1% with respect to signal intensity). These facts ensure the multispectral ability of the present scheme. Advantage of the present multi-wavelength method is explained later by showing the results of two species.

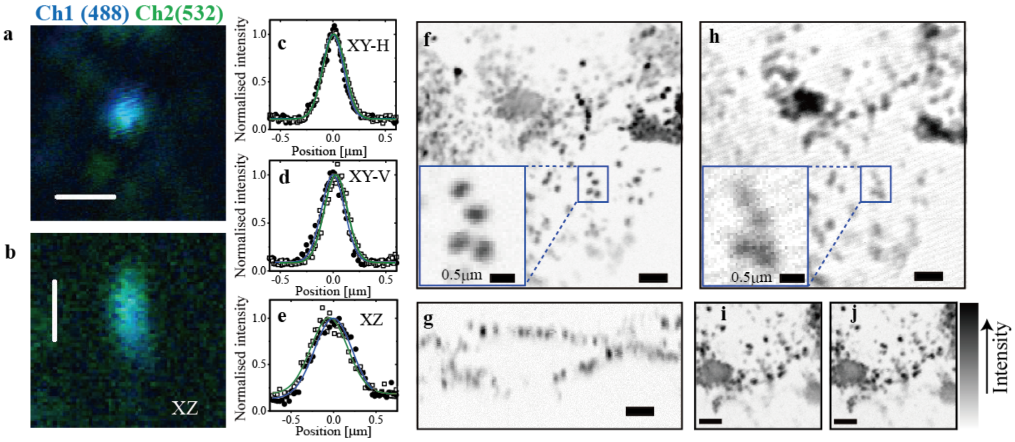

Fig. 2. Photothermal images of signal gold nanoparticle and label-free 3D imaging of mouse melanoma tissue section. (a, b), Combined images of a 20-nm gold nanoparticle embedded in polyvinyl alcohol with excitation at 488 nm (blue) and 532 nm (green). The wavelengths of the two pump beams overlapped the absorption spectrum of the gold nanoparticles due to plasmon resonance with a peak at 524 nm. The 488-nm and 532-nm pump beams were modulated at 1.07 and 1.1 MHz, respectively, and the probe beam was modulated at 1.0 MHz. The time constant of the lock-in amplifier was 1 ms, and the pixel dwell time was 2 ms. Scale bars, 500 nm. (c, d), Intensity profiles of the single nanoparticle with excitation at 488 nm (filled circles) and 532 nm (open squares) in the horizontal and vertical directions, respectively. For the 488-nm pump beam, fitting of a single particle with the Gaussian (solid curves) gives the full-width at half-maximum (FWHM) values of 234 nm and 249 nm in the horizontal and vertical directions, respectively. For the 532-nm pump beam, the FWHM values are 256 nm and 257 nm in the horizontal and vertical directions, respectively. (e), Intensity profiles along the axial direction. FWHM values are 525 nm and 510 nm for the 488-nm and 532-nm pump beams, respectively. (f, g), Photothermal images of a slice of mouse melanoma in the lateral and axial planes, respectively. Time constant of the lock-in amplifier was 0.5 ms, and pixel dwell time was 1 ms. The pump and probe beam powers incident on the sample were 50 and 150 μW, respectively. A set of 30 images of a slice of mouse melanoma is subsequently acquired by changing the sample position in the axial direction with a step size of 0.28 μm (see Media 1). Each image size is 19.6 x 19.6 μm at 200 x 200 pixels. (h) Bright field image of slice of mouse melanoma in the same area as in (f). (i,j) Photothermal images in the simultaneous measurement with excitation at (i) 488 nm and (j) 532 nm . Scale bars, 2 μm in (f-j) and 0.5 μm in the inset of (f, h).

3.2 Simultaneous dual-wavelength imaging

We demonstrated dual-wavelength photothermal imaging of a biological tissue slice stained with H&E, a popular staining method widely used in histology and histopathology. Hematoxylin is nonfluorescent, whereas eosin is fluorescent with a quantum yield of 10-20% [22]. Although the absorption spectra of hematoxylin and eosin overlap [Fig. 3(a)], their intensities depend on the wavelength: hematoxylin absorbance at 532 nm is 1.8 times larger than that at 488 nm, whereas eosin excitation efficiency at 532 nm is 2.3 times larger than that at 488 nm. This difference allows us to unmix the two channel images to determine the distribution of each species. Here, the absorption spectrum of eosin is calculated from the excitation spectrum of eosin contained in the specimen. The magnitude of the excitation spectrum is related to the molar absorption coefficient by assuming that fluorescence quantum yield does not depend on the excitation wavelength because of the Kasha's rule and that the area of absorption spectrum of eosin in the specimen is nearly equal to that in aqueous solution.

Figures 3(b) and 3(c) show photothermal images of a part of a rabbit oocyte with excitation at 488 nm and 532 nm, respectively. Both pump beam powers were set to be sufficiently weak (40 μW) to avoid saturated excitation. Figure 3(d) shows a blight field image of the tissue in the same area as that in Figs. 3(b) and 3(c). The same objective lens and a doublet lens are used to produce the image on a CCD with a white LED backlight. Linear spectral unmixing was then performed [Fig. 3(e)–3(g)], in which pseudo-colored blue and red denote the abundance of hematoxylin and eosin, respectively. In the linear spectral unmixing process, the absorption spectra of hematoxylin and eosin [Fig. 3(a)] are used as reference spectra. The residual spatial displacement between the two channels is not calibrated because it is smaller than the 100-nm pixel step size. The figure clearly shows that a granule cell is stained with hematoxylin while the zona pellucida and cytoplasm are stained with eosin. We also measured sectional (XZ) images [Fig. 3(h)–3(j)] and found that tissue morphology is clearly visualized in the depth direction.

As fluorescence comes only from eosin, it is helpful to detect fluorescence to verify the results of the spectral unmixing. Figure 3(k) shows the combined image of confocal fluorescence (green) and photothermal (red) signals. Here, only the 488-nm beam was used for pumping. Photothermal and fluorescence signals are simultaneously measured during the sample scan (multimodal imaging). Scanning area is the same as that in Figs. 3(b) and 3(c). We confirm that intense fluorescence is detected from the zona pellucida and cytoplasm, while nearly uniform and weak fluorescence is detected from the granule cell, consistent with the images of Figs. 3(e)–3(g). The position of the maximum of the fluorescence signal and that of the photothermal signal seems to be slightly shifted by ~0.5 μm in the depth direction [23].

The degree of cross-talk between the unmixed images in Fig. 3 is evaluated by calculating a factor

$$\gamma_{\mathrm{h/e}} = \iint S_{\mathrm{h}}(x,y) / S_{\mathrm{e}}(x,y) dxdy, \tag{1}$$

where $S_{\mathrm{h(e)}}(x,y) = s_{\mathrm{h(e)}}(x,y)/s_{\mathrm{h(e)}}^{\max}$ with $s_{\mathrm{h(e)}}(x,y)$ the intensity at the position (x, y) and $s_{\mathrm{h(e)}}^{\max}$ the maximum intensity in the unmixed image for hematoxylin (eosin). Integration is performed over the zona pellucida and cytoplasm domains by assuming that they are stained only by eosin, which results in $\gamma_{\mathrm{h/e}}$ of ~6%.

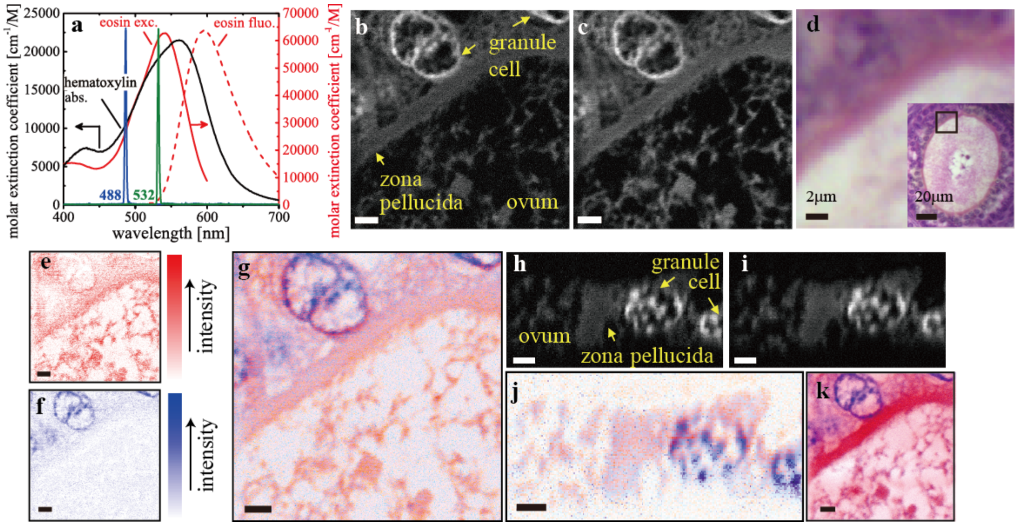

Fig. 3. Dual-wavelength photothermal images of hematoxylin and eosin (H&E) stained biological tissues (a), Absorption (red solid curve) and fluorescence (red dot-dashed curve) spectra of eosin and absorption spectrum of hematoxylin (black solid curve). Laser wavelengths of the two pump beams are also shown. (b, c), Photothermal images of H&E-stained rabbit ovary slice with excitation at 488 nm and 532 nm, respectively. Probe beam power was 300 μW. Image size was 19.6 x 19.6 mm with 300 x 300 pixels. The time constant of the lock-in amplifier was 0.5 ms, and the pixel dwell time was 1 ms. Image acquisition time was ~120 s. (b) Bright field image of the tissue in the same area as that in (c,d). The inset is the entire picture of the oocyte. (e, f), Unmixed images reflecting the distribution of eosin (red) and hematoxylin (blue), respectively. (g), Dual-wavelength image produced by combining images e and f. (h, i), Cross-sectional images of a slice of rabbit ovary with excitation at 488 nm and 532 nm, respectively. Image size was 19.6 x 9.8 mm with 200 x 100 pixels, Image acquisition time was ~30 s. (j), Unmixed image reflecting the distribution of eosin and hematoxylin. (k), Combined image of photothermal (blue) and fluorescence (red) signals. Scale bars, 2 μm.

3.3 Collection angle and modulation frequency dependence

To ensure that the observed signal is not affected by other pump-probe signals such as stimulated emission or excited state absorption, we examined the relation between collection angle of the transmitted probe beam and signal intensity. When the photothermal signal is detected in the forward (transmission) configuration, the measured signal arises from the interference between the scattered field due to photothermal effect and the transmitted diverting probe field [2, 14]. In this case, the signal is most intense when the numerical aperture of the condenser lens (NA_c) is smaller than that of the focusing lens. We found that the signal is most intense at NA_c ~0.6, and the experimental result fairly agrees with the curve calculated based on the scattering theory with modulated Yukawa potential [14] (Fig. 4). This characteristic behavior suggests that the measured signal is attributable to the photothermal effect.

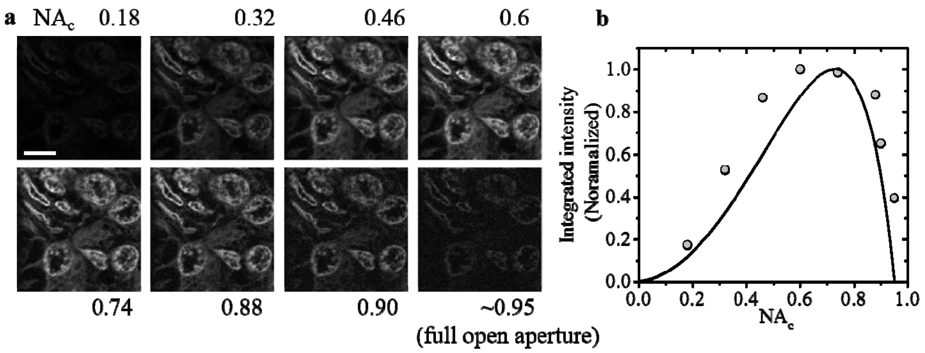

Fig. 4. Relation between the signal intensity and collection angle of the probe beam. (a), Images of a slice of rabbit kidney stained with hematoxylin and eosin with various values of the numerical aperture of the condenser lens system (NA$_c$). Scale bar, 5 µm. (b), Integrated intensity as a function of the NA$_c$. The theoretical curve (solid curve) is calculated using Eq. (15) in Ref [14]. with $r_c = 0.2$ µm.

Furthermore, the frequency response of the signal is measured by synchronously varying the modulation frequencies of pump and probe beam while holding the frequency difference at 15 kHz. In photothermal microscopy, signal intensity decreases when the spatial extent of the modulating refractive index is smaller than the focal spot size, and the cutoff frequency is thus estimated to be several MHz assuming a thermal diffusivity of ~0.1 mm^2/s. We verified that the signal intensity (magnitude) decreased by half at ~1 MHz and the phase approaches π/2 as the modulation frequencies increase (Fig. 5). The π/2 out of phase component comes from the retardation effect in heat conduction [2, 15]. Thus, the phase images offer the possibility of analyzing thermal diffusivity in tissues and would be useful to study the effects of heat transport in biological tissues.

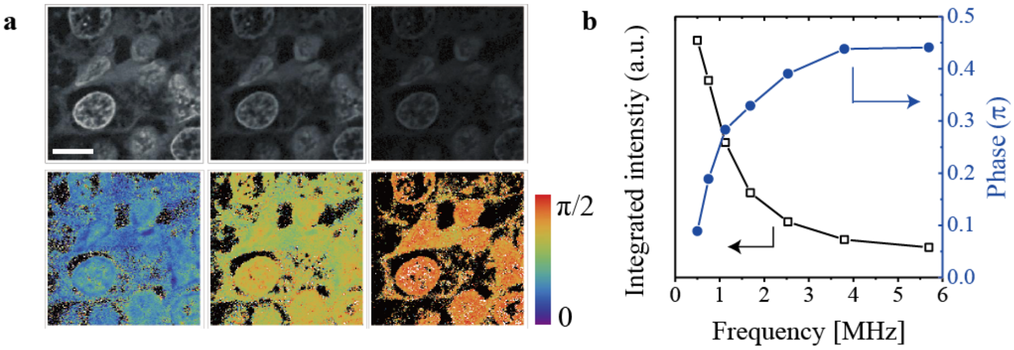

Fig. 5. Modulation frequency dependence in photothermal microscopy. (a), Intensity (upper) and phase (lower) images of a slice of rabbit kidney stained with hematoxylin and eosin with excitation at 488 nm. Modulation frequencies of the pump beam are 0.5, 1.13, and 2.53 MHz (from left to right), respectively. Scale bars, 5 µm. (b), Integrated intensity and averaged phase as a function of modulation frequency of the pump beam.

4. Discussion

Although both fluorescent and nonfluorescent materials can be detected in photothermal microscopy because they release heat through vibrational relaxation, nonfluorescent molecules are more suited for (multi-wavelength) imaging because fluorescent molecules are easily damaged or quenched through a triplet state as they have longer excited state lifetime compared with a short lived nonfluorescent molecule. In this regard, eosin has a quantum yield for triplet state formation of about 70% [22], and an increase in pump power easily induces saturated excitation. These saturation effects would cause an error in performing

#228731 - $15.00 USD Received 28 Nov 2014; revised 19 Jan 2015; accepted 26 Jan 2015; published 5 Feb 2015

linear spectral unmixing. Furthermore, the light to heat conversion efficiency of nonfluorescent material is usually better than that of fluorescent material. In the measurement of H&E stained sample, we confirmed that there was minimal damage to a part of tissue stained by hematoxylin, while eosin is slightly bleached after several measurements.

The simultaneous measurement with linear unmixing is considered to be much less affected by photobleaching compared with the frame-by-frame measurement. This can be explained as follows. The photothermal signal for the *i*th pump channel S_i is given by the linear sum of the signals from the different species

$$S_i \propto \sum_j^2 I_i \sigma_j(\lambda_i) c_j, \tag{2}$$

where I_i is the intensity of the *i*th pump beam ($i = 1,2$), $\sigma_j(\lambda_i)$ is the absorption cross section of the *j*th species at the wavelength λ_i, and c_j is the concentration of the *j*th species. To take into account the effect of photobleaching, average concentration c_j' is used for time varying c_j during the measurement. This does not give serious errors because of the weak degradation of eosin (< 20%). In the simultaneous measurement, linear unmixing can be performed using two values (S_1 and S_2) with the same c_j' since it is the same for the two pumping processes at λ_1 and λ_2. In contrast, in the frame by frame measurement, c_j' changes with repeated scan and is different from channel to channel. This would cause an error in unmixing calculation. Therefore, the simultaneous measurement is crucial for multi-wavelength imaging.

In the experimental setup, two pump beams were collimated with different SM fibers to avoid the effect of residual chromatic aberration of a doublet lens placed after the SM fiber on the focal position. However, all beams could be collimated through a single SM fiber without chromatic aberration if a reflective collimator is employed. This could dramatically simplify the system and eliminate the need to independently adjust the laser beams.

Finally, we consider the detection limit of the photothermal microscopy. The magnitude of the modulating refractive index at the focal volume is approximated by

$$\Delta n \sim \frac{N\sigma P}{sfC\rho r_c^3}\frac{\partial n}{\partial T}, \tag{3}$$

where N is the number of molecules in the focal volume, σ ($\sim 10^{-16}$ cm^2) is the absorption cross-section of dye molecules, P (~100 μW) is the pump beam power, s ($\sim 10^{-9}$ cm^2) is the beam waist area, f (~1 MHz) is the modulation frequency, C [~1 J/(gK)] and ρ (~1 g/cm^3) are heat capacity and density of the medium, respectively, r_c is the spatial extent of the modulating refractive index ($r_c^3 \sim 10^{-14}$ cm^3), and $\partial n / \partial T$ ($\sim 10^{-4}$ K^{-1}) is refractive index variations by temperature increase. Assuming that the relative change in probe beam transmissivity and Δn is of the same order of magnitude, and the noise level of the probe beam is nearly shot-noise limit ($\delta P'/P' \sim 1 \times 10^{-5}$ when the time constant of the lock-in amplifier is 0.5 ms), the detection limit (number of molecules when SNR is unity) is calculated to be $N' \sim 10^2$-10^3. This is consistent with the experimental results of a 20 nm-sized gold nanoparticle, whose absorption cross section is $\sim 10^{-12}$ cm^2 and SNR is $\sim 10^2$. Since σP is wavelength dependent, the detection limit in the dual-wavelength photothermal microscopy is determined by a smaller value of σP in either of the channels.

5. Conclusion

Simultaneous dual-wavelength imaging have been demonstrated by simply incorporating LDs with different wavelengths. The advantages of photothermal microscopy implemented with this scheme are (1) subdiffraction resolution by ~30% with optical sectioning capability, (2) applicable to both non-fluorescent materials and fluorescent systems even at the same time, (3) multicolor and multimodality. Thus, this method would be widely useful in biological and medical imaging.

Acknowledgments

This study was financially supported by a Grant-in-Aid for Scientific Research (No. 24740261) received from the Japan Society for the Promotion of Science and a joint research project at the Institute of Laser Engineering, Osaka University, under contract number B1-27.